

## Role of Electrostatic Interactions on Engineering Reaction Barriers: The Case of CO Dissociation on Supported Cobalt Particles

Wai-Leung Yim and Thorsten Klüner\*

*Institut für Reine und Angewandte Chemie, Theoretische Chemie, Carl von Ossietzky Universität Oldenburg, Carl-von-Ossietzky-Strasse 9-11, 26129 Oldenburg, Germany*

Received June 24, 2008

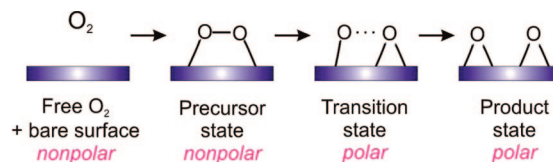
**Abstract:** We demonstrate a systematic optimization of the activation barrier of CO dissociation on cobalt surfaces on the basis of a chemical bonding picture of the corresponding transition structures. In particular, Co clusters adsorbed on MgO(100), graphene, and carbon nanotubes have been investigated. We discovered that the C–O moiety has a polar covalent character at the transition state which is feasibly stabilized by electrostatic interactions. This can be realized by replacing the  $\beta$ -Co atom with a less electronegative transition metal atom. The effect of 13 different substituting elements on CO dissociation has been investigated.

### Introduction

Modern experimental and theoretical methods have been used for understanding elementary industrial processes, such as CO oxidation,<sup>1–3</sup> CO activation,<sup>4,5</sup> oxygen reduction reaction (ORR),<sup>6–8</sup> and olefin metathesis.<sup>9</sup> In particular, the investigations can be consolidated by multiphysics approaches, e.g. using surface science techniques and first-principles calculations.<sup>10–12</sup> The knowledge thus obtained has impacted on the enhancement of power efficiency and the development of renewable energy resources.

Using modern apparatus, the screening of potential catalysts can be achieved without a detailed chemical understanding. For instance, a parallel screening of bimetallic catalysts for ORR was carried out using scanning electrochemical microscopy (SECM).<sup>13</sup> Despite this, the automatic screening process has certain limitations on the systems of great complexities, and detailed mechanistic studies on those cases would be desired. One of the examples is the CO-poisoning problem in fuel cells which is due to an inevitable contamination of hydrogen gas by carbon monoxide.<sup>14</sup> Another example is a debate about the initial activation mechanism in the Fischer–Tropsch (FT) process which converts CO and H<sub>2</sub> into liquid hydrocarbons using cobalt-containing catalysts: one proposed mechanism involved

**Scheme 1.** Electronic Interaction between O<sub>2</sub> and a Transition Metal Surface during the O<sub>2</sub> Dissociation Process



formation of C, O, and H adatoms, another one involved hydrogen-assisted C–O bond cleavage.<sup>15</sup>

First-principles calculations were proven to be powerful to resolve the influencing factors in the complicated processes. Based on the computed energetics results, the relative importance of reaction channels can be estimated, and the underlying mechanism can be rationalized by chemical bonding analyses. Recently, we have discovered that the short-range electrostatic effects were significant in tailoring the O<sub>2</sub> dissociation process, which was crucial for both the ORR and CO oxidation.<sup>8</sup> This was realized by a recent implementation of Bader analysis on charge density grids generated by planewave DFT calculations.<sup>16,17</sup>

The stabilization mechanism is illustrated in Scheme 1. The O<sub>2</sub> molecule exhibits no dipole moment in gas phase. Surprisingly, the O<sub>2</sub>-species at the transition structure showed a considerable polar character.<sup>17</sup> So, an embedded ion at the reactive site can stabilize the transition state, while the precursor state is less affected. As a result, the O<sub>2</sub> dissociation

\* Corresponding author phone: +49-441-798-3681; fax: +49-441-798-3964; e-mail: thorsten.kluener@uni-oldenburg.de.

barrier can be manipulated. Short-range electrostatic effects may also be important for the gas reformation on the polarizable transition metal oxide substrates, such as ZnO,<sup>18</sup> and further confirmation will be required.

In this study, we examine the electrostatic effects on the CO activation on both cobalt nanoparticles and flat cobalt surfaces. In the case of CO, the carbon atom would be more negatively charged in the course of the dissociation process. Therefore, the CO activation is affected by the electrostatic effects. Similar effects for various adsorbate/substrate systems have been reported in the literature.<sup>19–32</sup> We selected a series of dopants of various electronegativities and found that the larger electronegativity difference between the doping element and cobalt was the stronger the stabilizing effect turned out to be. Our study illustrates the promoter effect by doping a reducing atom, which paves the way to enhance the efficiency of CO activation. Nevertheless, catalytic CO-activation is mechanistically very complicated, and our results can only be regarded as model studies in particular given the fact that we try to identify quite simple, i.e. electrostatic mechanisms. Although reality might be much more complex, we hope that this work stimulates further computational studies. Open questions concern the observation that the Pd-promoter effect is currently found not to be due to electrostatic interactions and the promoting behavior of Pd is not known yet.<sup>33</sup>

## Computational Details

**Model.** For isolated clusters, a  $15 \times 15 \times 15 \text{ \AA}^3$  cubic supercell with  $\Gamma$ -point sampling has been used. For supported clusters, we considered graphene, (6,6) single-walled carbon nanotube (SWNT), and MgO(100) as supports. For the cluster/graphene system, we used a hexagonal supercell ( $a = 12.2 \text{ \AA}$  and  $c = 16.0 \text{ \AA}$ ), with a  $2 \times 2 \times 1$  Monkhorst-Pack (MP) mesh for k-space integration. For the cluster/(6,6) SWNT system, we used an orthorhombic supercell ( $18.0 \times 23.9 \times 12.3 \text{ \AA}^3$ ) with a  $1 \times 1 \times 2$  MP k-point mesh. For the cluster/MgO(100) system, we used three layers of MgO in a tetragonal supercell ( $a = 12.0 \text{ \AA}$  and  $c = 20.3 \text{ \AA}$ ) with a  $2 \times 2 \times 1$  MP k-point mesh. For each system, systematic convergence checks were performed with respect to slab thickness, k-point sampling, and cutoff.

To study CO dissociation on pure and substituted Co(0001) surfaces, we used a  $(3 \times 3)$  Co(0001) surface slab of three atomic layers in a hexagonal supercell ( $a = b = 7.47 \text{ \AA}$ ,  $c = 8 \text{ \AA}$ ). A  $2 \times 2 \times 1$  MP mesh was chosen for k-space integration. The optimized structure of Co(0001)-CO was taken as a starting configuration of a MD-simulation, in which the sample was heated to 300 K for 250 fs, and then a constant temperature MD trajectory was calculated for a total simulation time of 1 ps, using Nosé-Hoover thermostat and a time step of 0.5 fs.<sup>34</sup> Constrained MD simulations were carried out subsequently, with the C–O distance of 1.2, 1.5, 1.8, 2.1, and 2.4  $\text{\AA}$ . Each trajectory was propagated at 50 K for 250 fs. The structure at the end of the last trajectory was optimized, and the minimum energy path was located by the climbing-NEB scheme.

**Theory.** We used the Vienna Ab Initio Simulation Package (VASP)<sup>35–38</sup> to perform spin-polarized DFT calculations.

The PBE exchange-correlation functional within the generalized gradient approximation (GGA) was chosen.<sup>39</sup> Pseudopotentials constructed by the PAW method were adopted.<sup>40</sup> The planewave and augmentation charge cutoffs were set to 400 and 645 eV, respectively. Geometry optimizations were carried out by the conjugate gradient scheme in VASP. The geometrical parameter space was explored by starting at different initial cluster orientations and adsorption sites. The convergence threshold was set to  $10^{-4}$  eV for both electronic structure calculations and geometry optimizations. The climbing-Nudged Elastic Band scheme was employed to search for transition structures.<sup>41,42</sup> Methods of charge topology analyses are referred to refs 16 and 17.

## Results and Discussion

To illustrate the electrostatic effects on CO activation, we model the cobalt surfaces by using an icosahedral Co<sub>13</sub> particle because of its small size and thermal stability.<sup>43,44</sup> We calculated the CO dissociation process on a bare Co<sub>13</sub> particle starting from their chemisorbed forms. On the surface of the bare Co<sub>13</sub> particle, CO adsorbs on a 3-fold hollow site with a chemisorption energy of  $-2.22$  eV. The CO dissociation is slightly exothermic by 0.21 eV with a barrier of 1.89 eV. The apparent barrier, relative to the isolated reactants, is negative which means that the activation energy of the dissociation is smaller than the chemisorption energy of CO on the surface ( $|E_a| < |E_{\text{chemil}}|$ ).

We have explored the substrate effects on the CO activation, by studying the reaction on the Co<sub>13</sub> particle deposited on several substrates—graphene, (6,6) single-walled carbon nanotube (SWNT), and MgO(100). The Co<sub>13</sub> particles on graphene-like substrates, graphene sheet and SWNT, have been considered. The strength of the Co<sub>13</sub>-graphene interaction is considerable, resulting in an interaction energy of  $-1.55$  eV. The Co<sub>13</sub> particle exhibits an even stronger interaction with a (6,6)-SWNT surface ( $-2.35$  eV). This fact is due to the enhanced reactivity with increasing surface curvature of the SWNT surface as compared to a flat graphene sheet.<sup>45</sup> In both cases, the net spin population was reduced by about 20% as compared with the free cobalt particle. Interestingly, despite strong interactions between the Co<sub>13</sub> particles and graphenic surfaces, the CO dissociation barriers are only slightly reduced by 0.06–0.14 eV (cf. Table 1). Furthermore, the minor role of graphenic substrates was confirmed by substrate deformation, where the mechanical force changes the barrier height by only 0.05 eV on Co<sub>13</sub>/graphene, and the effect is negligible ( $\pm 0.01$  eV) on Co<sub>13</sub>/(6,6)-SWNT.

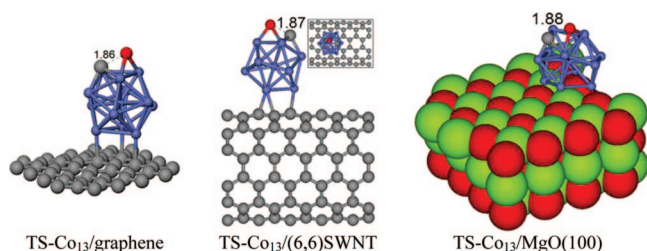
We also examined CO dissociation on an ionic MgO(100) support for comparison. The Co<sub>13</sub> particle is strongly bound to the MgO(100) surface, with an adsorption energy of  $-3.78$  eV. The Co atoms are mainly attached to the oxygen sites of MgO, which is in accord with a former study by Xu et al.<sup>46</sup> Due to the symmetry mismatch, the triangular facet of the Co<sub>13</sub> particle attached to MgO(100) is distorted and opened. On Co<sub>13</sub>/MgO(100), the CO dissociation barrier is further reduced to 1.69 eV. When the MgO(100) surface is compressed or stretched, the interaction with the distorted Co facet is changed: the barrier height is increased by 0.36

**Table 1.** Energetics of CO Dissociation on Supported Co<sub>13</sub>

	$\Delta E$ (eV) <sup>a</sup>	$E_a$ (eV) <sup>b</sup>	$\Delta E_a$ (eV) <sup>c</sup>
bare Co <sub>13</sub>	-0.21	1.95	-
Co <sub>13</sub> /graphene	-0.23	1.81	-
Co <sub>13</sub> /graphene <sup>d</sup>	-0.13	1.85	0.04
Co <sub>13</sub> /graphene <sup>e</sup>	-0.17	1.86	0.05
Co <sub>13</sub> /(6,6)SWNT	-0.02	1.89	-
Co <sub>13</sub> /(6,6)SWNT <sup>f</sup>	-0.04	1.88	-0.01
Co <sub>13</sub> /(6,6)SWNT <sup>g</sup>	0.03	1.9	0.01
Co <sub>13</sub> /MgO	-0.16	1.69	-
Co <sub>13</sub> /MgO <sup>h</sup>	0.16	2.05	0.36
Co <sub>13</sub> /MgO <sup>i</sup>	0.06	1.92	0.23

<sup>a</sup> Energy change:  $\Delta E = E[\text{C(ad)}\cdots\text{O(ad)}] - E[\text{CO(ad)}]$ .

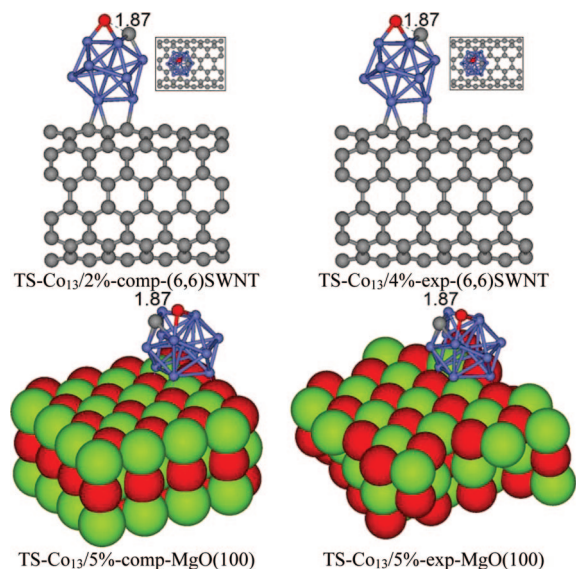
<sup>b</sup> Activation barrier:  $E_a = E(\text{TS}) - E[\text{CO(ad)}]$ . <sup>c</sup> Change of activation barrier ( $\Delta E_a$ ) is referenced to the Co<sub>13</sub> deposited on undistorted support. <sup>d</sup> 2% compression,  $E(\text{graphene})$  is increased by 3.0 eV/cell. <sup>e</sup> 4% expansion,  $E(\text{graphene})$  is increased by 2.3 eV/cell. <sup>f</sup> 2% compression,  $E(\text{SWNT})$  is increased by 1.4 eV. <sup>g</sup> 4% expansion,  $E(\text{SWNT})$  is increased by 5.1 eV. <sup>h</sup> 5% compression. <sup>i</sup> 5% expansion.

**Figure 1.** Transition structures of CO dissociation on supported Co<sub>13</sub> particles.

eV (5% compression) and 0.23 eV (5% expansion), respectively. These changes are more pronounced than those on Co<sub>13</sub>/graphenic surfaces.

To understand the trend of the CO dissociation barriers on different supported Co<sub>13</sub> particles, we illustrate the differences by showing the structural parameters and chemical bonding pictures of the transition structures. The precursor state contains a CO molecule adsorbing at the 3-fold hollow site of the Co<sub>13</sub> facet, while the C and O atoms as reaction products will adsorb at the hollow sites of the neighboring triangular facets. At the TS, the carbon atom has moved to the next-neighboring triangular facet and is coordinated to three Co atoms, while the O atom is adsorbed at the bridge site with the C–O distances ranging from 1.86 to 1.88 Å, respectively (cf. Figure 1). Interestingly, the structure of the transition state is virtually identical for bare and supported Co<sub>13</sub> particles, indicating that the influence of the support on the CO-dissociation barrier is not due to a simple structural deformation. The transition structures for CO dissociations on Co<sub>13</sub> particles supported by deformed substrates are also shown in Figure 2. All geometrical details of the adsorbed particles will be provided to the interested reader in the Supporting Information.

Instead, we found that the stabilization of the TSs was influenced by the surface polarity. We used the electron-localization-function (ELF)<sup>47</sup> and Bader analysis<sup>16,17,48</sup> to illustrate this phenomenon. The ELFs for the transition structures of CO dissociation on the supported Co<sub>13</sub> particles are shown in Figure 3. At the initial states, the hollow-site CO exhibits a localized orbital between the carbon atom and

**Figure 2.** Transition structures of CO dissociation on Co<sub>13</sub> on deformed supports.

the Co<sub>13</sub> surface, which refers to the 5σ orbital of CO. The 4σ-lone pair orbital localized on the oxygen atom of CO and the C–O bond are visible as well.

At the TSs, the C–O bonding character greatly changes (cf. Figure 3). The electrons surrounding the C and O atoms exhibit a spherical shape, without a significant electron density between the C and O atoms. This indicates that the polar covalent character of the C–O bond increases at the TS, which is further confirmed by characterizing bond critical points (BCPs).<sup>17,48</sup> On the supported Co<sub>13</sub> particles, the Laplacians of the electron density at the BCPs of C–O are positive, revealing a dominating polar covalent character between them (cf. Table 2).<sup>49</sup> Moreover, the C and O atoms are bonded to the Co<sub>13</sub> surfaces by polar covalent bonds.

In addition, the surface polarity at the TS is demonstrated by the electric charges and atomic dipoles (cf. Table 2).<sup>16</sup> At the TS, both C and O atoms carry a negative charge, which agrees with the finding of ELF. The magnitude of these charges is not sensitive to the choice of support since the differences are beyond the accuracy of a population analysis. In contrast, a significant influence of the support on the atomic dipole moments in the TS-structure can be observed. Comparing the oxygen atomic dipole moment of the CO-molecule on both supports in fact suggests that the difference of atomic dipole moments on the two substrates might be due to the significantly different electric field of the supporting materials.

By chemical intuition, the transition state can be stabilized by embedding positive ions at the surface, while the chemisorbed CO molecule is less affected due to its charge neutrality. As a result, the CO dissociation barrier is adjustable. As mentioned above, the CO dissociation barrier is slightly lower when Co<sub>13</sub> is deposited on the MgO(100) surface, as compared to the (6,6)-SWNT. By comparing the difference of the Laplacian of the density at the BCP, we identified that the bond number 3 was the most important in stabilizing the transition state (cf. Table 2).

We hypothesize that the CO dissociation barrier can be modified chemically by substituting a less electronegative



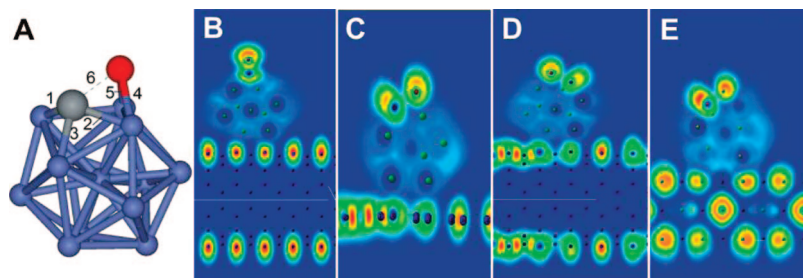


**Figure 3.** Contour plots of the electron localization function: [a] connectivity of CO/bare-Co<sub>13</sub> at the TS; [b] ELF of CO/Co<sub>13</sub>/(6,6)SWNT at the precursor state; [c] ELF of CO/Co<sub>13</sub>/graphene at the TS; [d] ELF of CO/Co<sub>13</sub>/(6,6)SWNT at the TS; and [e] ELF of CO/Co<sub>13</sub>/MgO at the TS.

**Table 2.** Properties of Bond Critical Points (BCPs) and Charge Distribution at Transition States<sup>a</sup>

bond	label	Co <sub>13</sub> /(6,6)SWNT		Co <sub>13</sub> /MgO(100)	
		$\rho_b$ (au)	$\nabla^2\rho$ (au)	$\rho_b$ (au)	$\nabla^2\rho$ (au)
Co–C	1	0.14	0.33	0.13	0.31
Co–C	2	0.15	0.36	0.16	0.36
Co–C	3	0.12	0.37	0.13	0.09
Co–O	4	0.09	0.58	0.09	0.54
Co–O	5	0.12	0.71	0.12	0.71
C–O	6	0.10	0.18	0.10	0.18

charge distribution					
label	Co <sub>13</sub> /(6,6)SWNT <sup>b</sup>		Co <sub>13</sub> /MgO(100) <sup>c</sup>		
	charge (e)	$\mu_{\text{atom}}$ (D)	charge (e)	$\mu_{\text{atom}}$ (D)	
Co atom	+0.17 <sup>d</sup>	1.11	+0.06 <sup>d</sup>	1.07	
C atom	−0.57	1.73	−0.56	1.60	
O atom	−0.84	0.25	−0.82	0.47	

<sup>a</sup> Atomic units are expressed as e bohr<sup>−3</sup> and e bohr<sup>−5</sup> for  $\rho_b$  and Laplacian, respectively. Atom numbering refers to Figure 3a. <sup>b</sup> (6,6)-SWNT, chemical formula: C<sub>120</sub>. <sup>c</sup> MgO(100), chemical formula: Mg<sub>48</sub>O<sub>48</sub>. <sup>d</sup> Average charge on Co atoms.

metal atom at the  $\beta$  position relative to the CO-attached cobalt facet. After substitution the geometry has been reoptimized using various initial structures which yield virtually identical results. We have selected transition metal elements of different groups and different periods of the periodic table, and also two main group elements (Li and Na), as shown in Table 3. From this, the effect of atomic/ionic size and electronegativity can be elucidated. It is noteworthy that we chose elements exhibiting a larger covalent radius than that of Co on purpose; otherwise, the core Co atom might move toward the surface and the skeleton of the model would be distorted.

Figure 4a reveals that the electronegativity of the substituting metal atoms plays an important role on the structure of the transition state and the modification of the corresponding energy barriers. When the difference in electronegativity relative to Co increases, the extent of stabilization will increase and the CO dissociation barrier height will decrease (cf. Figure 4a). The stabilization effect is also revealed by the Laplacian of the density: the more positive the Laplacian of the density at the BCP is, the smaller the dissociation barrier turns out to be.

We estimated the contributions of the electric monopoles and electric dipoles in the overall electronic interactions, by using the following formulas:<sup>50</sup>

**Table 3.** Energetics of CO Dissociation on Substituted M-Co<sub>12</sub> Particles

particle	$\Delta E$ (eV) <sup>a</sup>	$E_a$ (eV) <sup>b</sup>	$E_{\text{mono}}^c$ (1/4 $\pi\epsilon_0$ )	$E_{\text{dipole}}^d$ (1/4 $\pi\epsilon_0$ )	charge <sub>M</sub> (e)
LiCo <sub>12</sub>	−0.01	1.67			
NaCo <sub>12</sub>	−0.34	1.72			
YCo <sub>12</sub>	−0.15	1.45	−0.74	0.09	+1.34
LuCo <sub>12</sub>	−0.09	1.51	−0.78	0.09	+1.40
TiCo <sub>12</sub>	0.02	1.72	−1.02	0.12	+1.75
ZrCo <sub>12</sub>	0.09	1.66	−1.59	0.13	+2.42
HfCo <sub>12</sub>	0.14	1.61	−2.08	0.10	+2.80
MoCo <sub>12</sub>	−0.55	1.84	−0.49	0.07	+0.82
WCo <sub>12</sub>	−0.16	1.87	−0.61	0.07	+1.00
RuCo <sub>12</sub>	−0.48	1.79	−0.35	0.07	+0.14
OsCo <sub>12</sub>	−0.63	1.81	−0.35	0.07	+0.03
Co <sub>13</sub>	−0.21	1.89	−0.37	0.08	
PdCo <sub>12</sub>	0.07	2.14	−0.49	0.09	−0.41
PtCo <sub>12</sub>	−0.02	1.77	−0.58	0.07	−0.69

<sup>a</sup> Energy change:  $\Delta E = E[\text{C(ad)}\cdots\text{O(ad)}] - E[\text{CO(ad)}]$ .

<sup>b</sup> Activation barrier:  $E_a = E(\text{TS}) - E[\text{CO(ad)}]$ . <sup>c</sup> Energy contribution due to the electric monopole term at the transition state. <sup>d</sup> Energy contribution due to the electric dipole term at the transition state.

Monopole interaction:

$$E_{el}(R^{AB}) = \frac{Q^A Q^B}{4\pi\epsilon_0 R^{AB}}$$

Dipole interaction:

$$E_{el}(R^{AB}) = \frac{\mu^A \mu^B}{4\pi\epsilon_0 (R^{AB})^3} (\cos \chi - 3 \cos \alpha_A \cos \alpha_B)$$

$Q^A$  and  $Q^B$  are estimated by the net charges of the atoms. The definitions of other symbols are shown in Scheme 2. To calculate the dipole–dipole interaction, the charge density difference is used to obtain the net dipole moments. The calculated results are also shown in Table 3 and Figure 4b. The electrostatic interaction is mainly determined by the monopole term. This can also be reflected by the charges of the substituents. Consistent with our prediction, the dissociation barrier decreases with increasing electrostatic interaction. It is of particular interest that Pd, which exhibits a promoter effect, does not activate CO dissociation by electrostatic interactions. Some exceptions are observed in Figure 4b, including substituting the elements Y, Lu, and Pd, which will be explained below.

Some of the data points in Figure 4 do not lie along the trend-curve, where the cases of Li, Na, Pd, and Pt turn out to be exceptions. These cases have very different transition structures as shown in the insets of Figure 4. Other transition

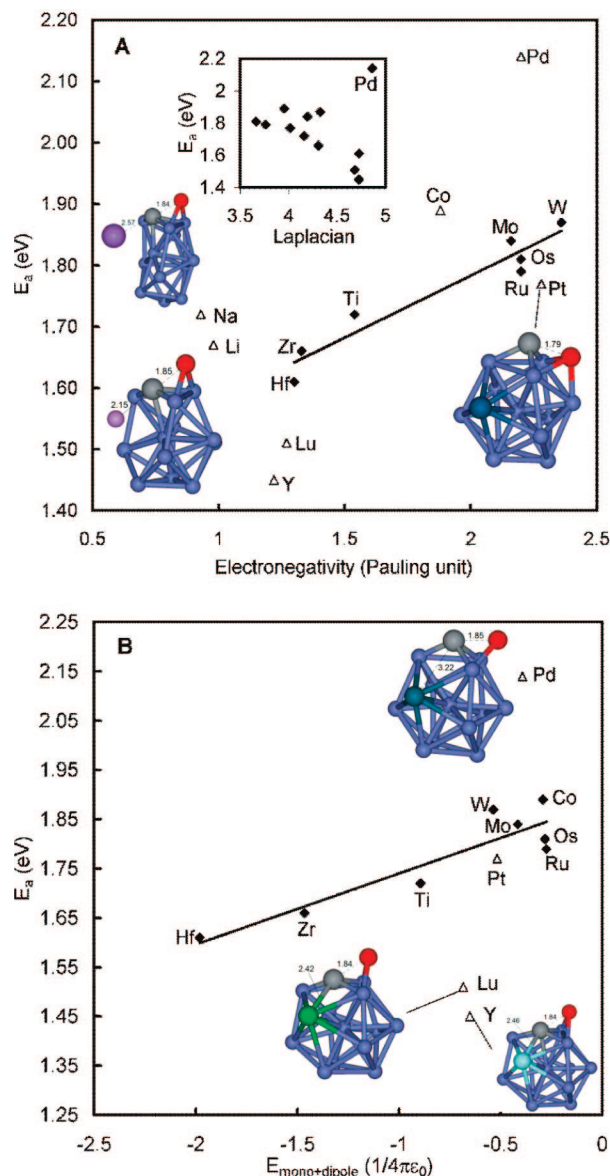
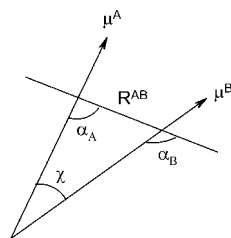


**Figure 4.** [a] Relation of dissociation barrier and the electronegativity of the substituted metal atom and [b] dependence of dissociation barrier on the electrostatic interactions.

**Scheme 2.** Parameters Required To Calculate the Energy Contribution Due to Monopole and Dipole Interactions



structures can also be found in Figure 5. In case of Li and Na, a charge transfer from the alkaline atom to the Co particle occurs, resulting in a significant distortion of the Co particle. For Pd and Pt, the C atoms are bonded to the hollow-site where the precursor-CO is located, instead of bonding to the  $\beta$ -Pd or the  $\beta$ -Pt atom, respectively. These structural differences explain the scattering of data points in Figure 4. Moreover, the barriers have been significantly reduced using

Lu and Y. When these two low-valent transition metal elements are used, the triangular facet of  $M\text{-Co}_{12}$  can be opened which is attributed to the weaker M-Co covalent interaction. As a result, the C atoms have higher coordination at the TS structures, leading to increased stability.

The abovementioned chemical tailoring is applied to the doped  $M\text{Co}_{12}$  model. Under experimental conditions, however, the assumed structural skeleton may be distorted depending on the thermal stability of the nanoparticles. We have used *ab initio* molecular dynamics simulations to test the structural stability of the particles. In these simulations, the optimized geometry was heated to the desired temperature (300 or 500 K) for 1 ps, followed by a longer molecular dynamics simulation for 10 ps using a Nosé-Hoover thermostat.<sup>34,51</sup> The time interval was set to 2 fs.

Our prediction of CO dissociation on icosahedral particles is valid in the low-temperature regime (300 K) (cf. Figure 6); at higher temperature (500 K), the nanosized particles exhibit different structures (cf. Figure 7). Nevertheless, the unravelled stabilization mechanism of CO at the transition state should be applicable for other surfaces of different morphology as well.

We have also considered the flat Co surfaces of different chemical composition. In detail, we selected Hf-, Lu-, Y-, and Zr-substituted Co(0001) surfaces, as these dopants exhibited a larger promoter effect on the CO activation on substituted- $\text{Co}_{13}$  particles. Here, the surface slabs keep their structures at elevated temperature.

For comparison, we have calculated the reaction profile of the CO dissociation on the pure  $(3 \times 3)\text{-Co}(0001)$  surface (cf. Table 4 and Figure 8). In this case, the chemisorbed CO exhibits a dissociation barrier of 2.47 eV, forming C(ad) and O(ad), and the corresponding reaction energy is found to be 0.93 eV. Compared to the energetics of CO dissociation on the  $\text{Co}_{13}$  particle, the barrier and reaction energy of CO dissociation on the flat Co(0001) surface are raised by 0.58 and 1.14 eV, respectively. The enhanced reactivity of the  $\text{Co}_{13}$  particle is due to its higher curvature where the effect is even more pronounced in the product states [C(ad)···O(ad)]. Curvature effects can also be found on single-walled carbon nanotubes and low-coordinated transition metal surfaces.<sup>52,53</sup> In addition, the apparent barrier is found to be 0.71 eV, which is comparable to the previous theoretical value of 1.04 eV as reported on a  $(2 \times 2)\text{-Co}(0001)$  surface.<sup>15,54</sup>

In agreement with our prediction by the  $\text{Co}_{13}$  model, the CO dissociation barrier is significantly reduced on the substituted-Co(0001) surfaces (cf. Table 4). With a transition metal substituent, the barrier is significantly reduced by 0.76–1.14 eV, resulting in a negative apparent barrier varying from  $-0.1$  eV to  $-0.5$  eV. We have also found a correlation between the activation energies obtained from the substituted cobalt surfaces of different curvatures (cf. Figure 9). Interestingly, a nice correlation is observed among pure cobalt, Hf- and Zr-substituted cobalt surfaces, which supports our intuition that the CO dissociation barrier can be engineered by introducing a less electronegative transition metal atom.

The explanation as mentioned above for the extraordinary low CO dissociation barriers for  $\text{YCo}_{12}$  and  $\text{LuCo}_{12}$  can also

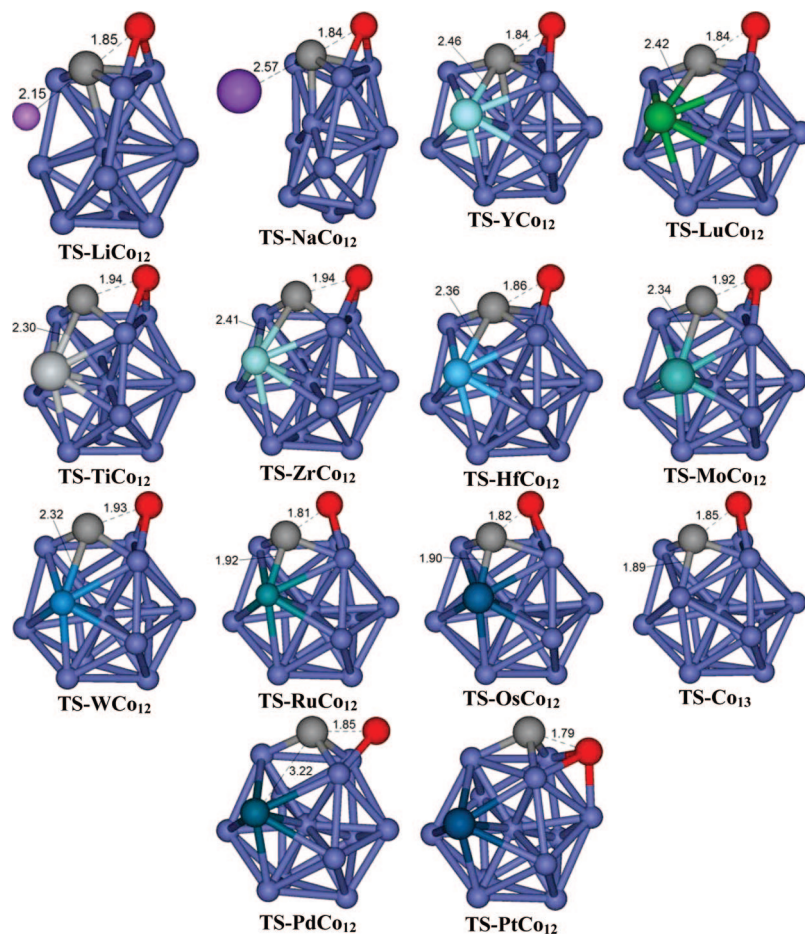


**Figure 5.** Transition structures for CO dissociations on  $M\text{Co}_{12}$  particles.

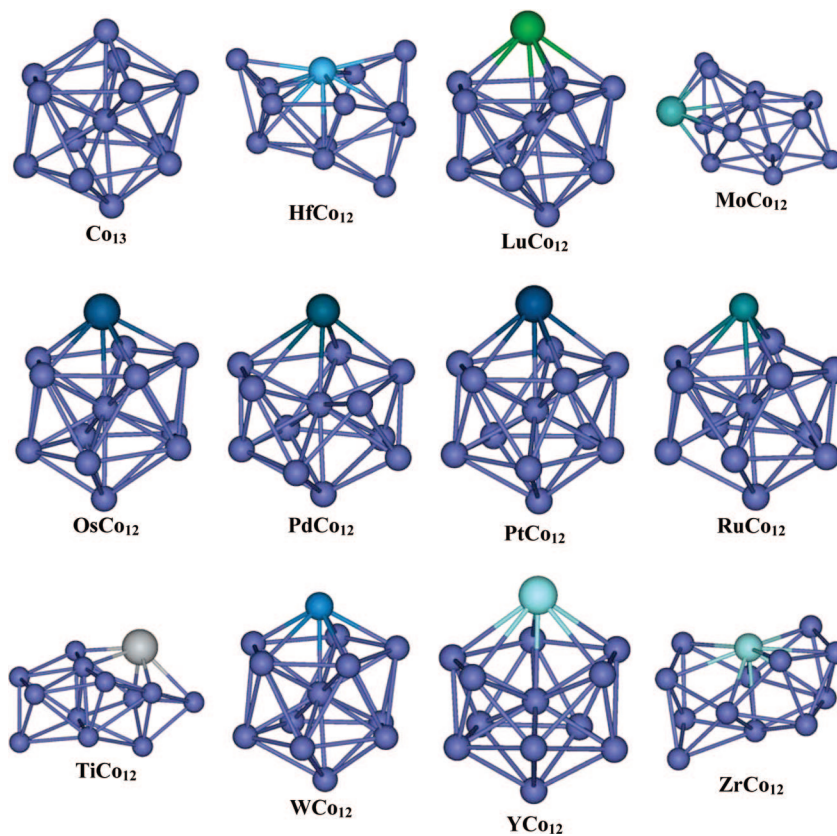


**Figure 6.** Structures of  $M\text{Co}_{12}$  particles after 300 K MD runs.



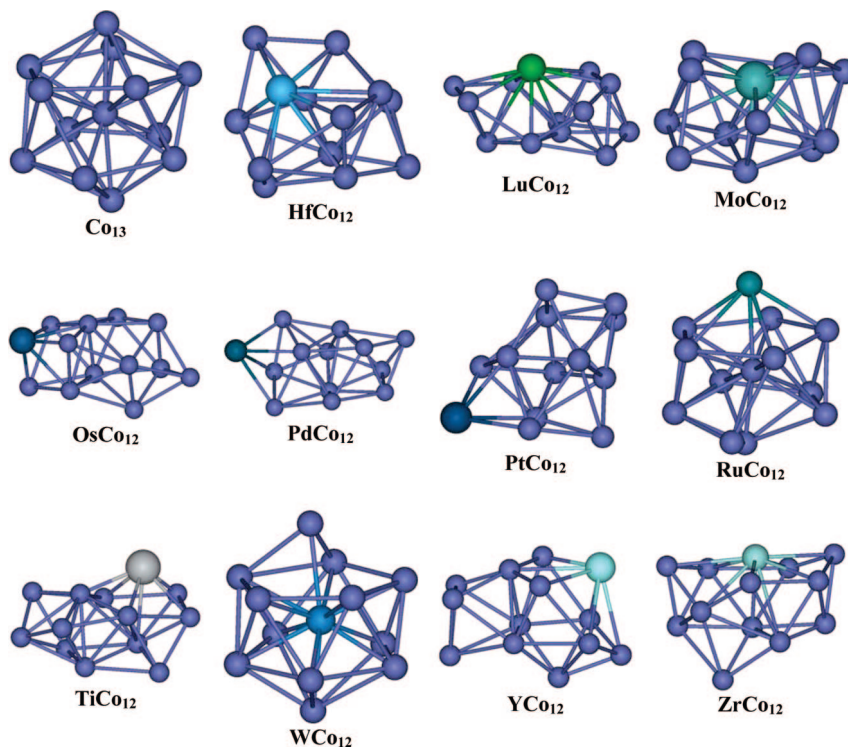


**Figure 7.** Structures of  $\text{MCo}_{12}$  particles after 500 K MD runs.

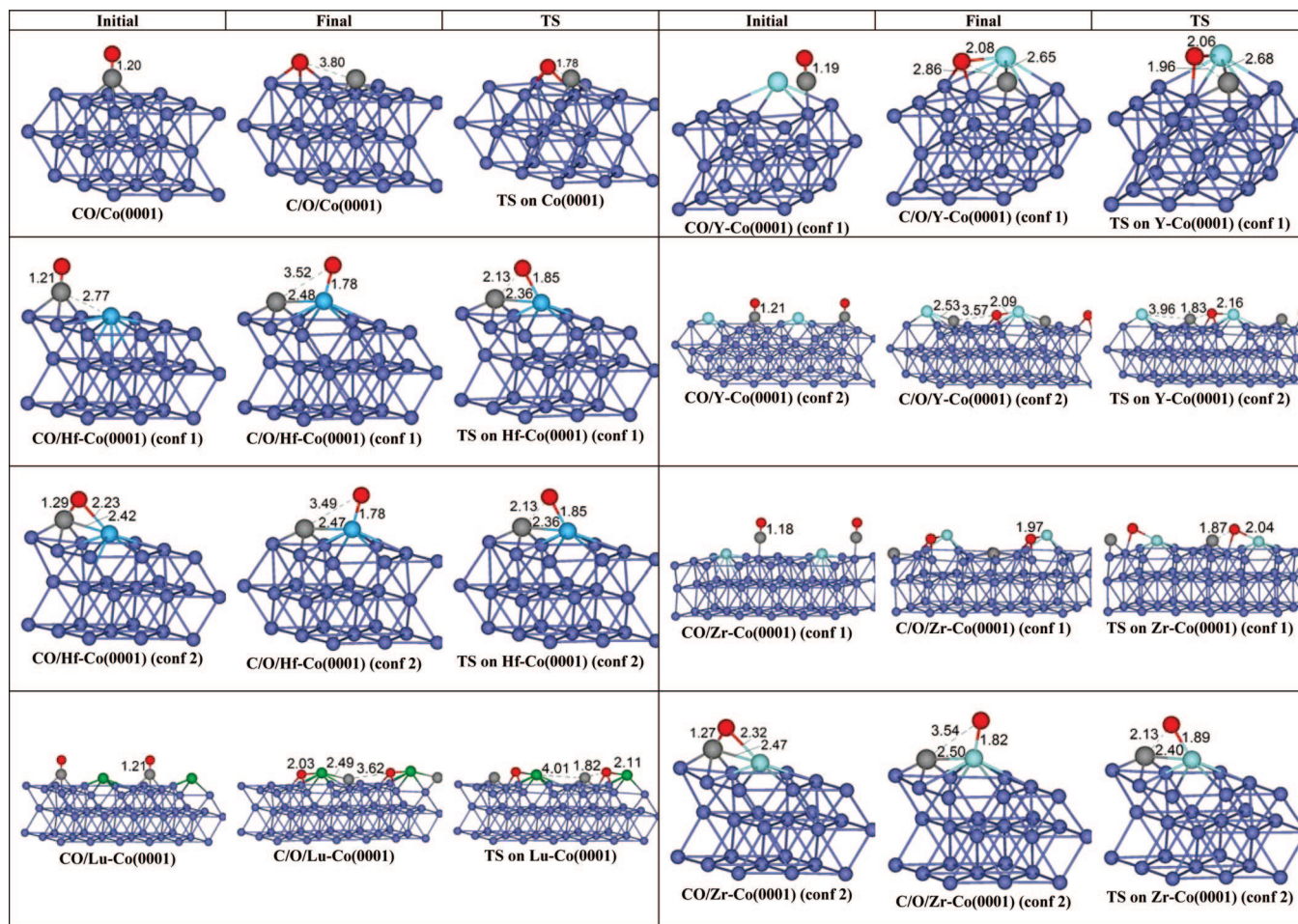


**Figure 8.** Initial, final, and transition structures for CO dissociations on substituted  $\text{Co(0001)}$  surfaces are shown in left, middle, and right columns, respectively.

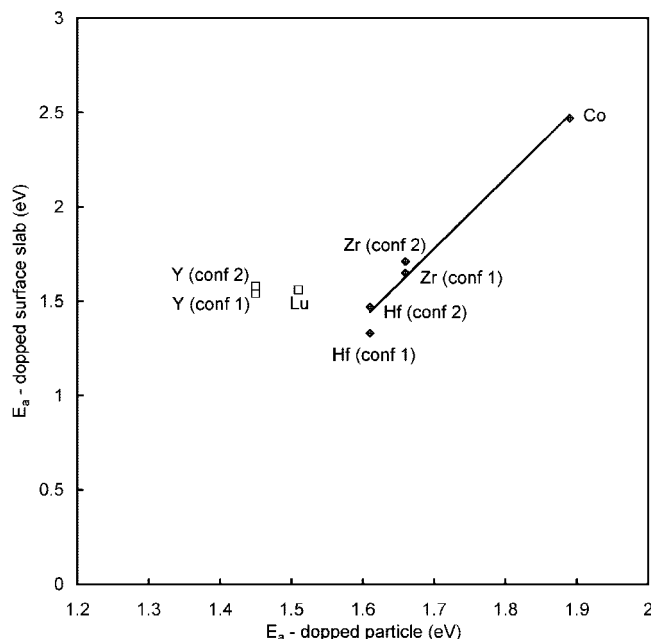


**Figure 9.**  $E_a$  (particle) vs  $E_a$  (flat surface).

**Table 4.** Energetics of CO Dissociation on Substituted Co(0001) Slabs

surface	$E_{\text{chemi}}$ (eV) <sup>a</sup>	$\Delta E$ (eV) <sup>b</sup>	$E_a$ (eV) <sup>c</sup>
pure Co(0001)	-1.76	0.93	2.47
Hf-Co(0001) (conf 1)	-1.83	0.84	1.33
Hf-Co(0001) (conf 2)	-1.97	0.98	1.47
Lu-Co(0001)	-1.82	-0.27	1.56
Y-Co(0001) (conf 1)	-1.76	0.17	1.54
Y-Co(0001) (conf 2)	-1.83	-0.27	1.58
Zr-Co(0001) (conf 1)	-1.75	0.40	1.65
Zr-Co(0001) (conf 2)	-2.01	1.17	1.71

<sup>a</sup> Chemisorption energy:  $E_{\text{chemi}} = E(\text{CO-surface}) - E(\text{free CO}) - E(\text{bare surface})$ . <sup>b</sup> Energy change:  $\Delta E = E[\text{C(ad)} \cdots \text{O(ad)}] - E[\text{CO(ad)}]$ . <sup>c</sup> Activation barrier:  $E_a = E(\text{TS}) - E[\text{CO(ad)}]$ .

be used for the scattered data of Y- and Lu-substituted cobalt surfaces. It should be mentioned that the minimum energy pathways lead to different oxygen coordination in the product states. For Y- and Lu-substituted Co(0001) surfaces, the oxygen adatoms occupy the hollow sites of the triangular Y-Co-Co and Lu-Co-Co facets, respectively, while the oxygen adatoms occupy the on-top sites of the dopants of other substituted-Co(0001) surfaces. Therefore, the CO dissociation reactions are found to be exothermic on the models Lu-Co(0001) and Y-Co(0001) (conf 2) but endothermic on other models.

## Conclusion

In conclusion, we performed large-scale DFT calculations to study the CO activation on Co<sub>13</sub> particles. We discovered the role of electrostatic interactions on stabilizing the transition states, while the initial structures were less affected due to the charge neutrality of the adsorbed CO-molecule. Our results revealed a controllable CO activation by replacing the  $\beta$ -Co atom. This strategy is also applicable on substituted-Co(0001) surfaces. In addition, as shown in this work, the Pd-dopant (one of the promoters in the FT process)<sup>2</sup> is unable to activate the CO dissociation via electrostatic effects. This

motivates a further investigation on the CO activation mechanism on Pd-doped cobalt surfaces, and a detailed mechanistic study is currently being undergone in our group.

**Acknowledgment.** We thank financial support from Fonds der Chemischen Industrie, Alexander von Humboldt Foundation (W.L.Y.), Hanse Wissenschaftskolleg (W.L.Y.), and the EWE AG (T.K.). The simulations were performed on the national supercomputer NEC SX-8 at the High Performance Computing Center Stuttgart (HLRS) under the grant number WLYIM.

**Supporting Information Available:** All geometrical details of the adsorbed particles. This material is available free of charge via the Internet at <http://pubs.acs.org>.

## References

- (1) Bond, G. C.; Thompson, D. T. *Catal. Rev. - Sci. Eng.* **1999**, *41*, 319.
- (2) Diehl, R. D.; McGrath, R. *Surf. Sci. Rep.* **1996**, *23*, 43.
- (3) Alavi, A.; Hu, P. J.; Deutsch, T.; Silvestrelli, P. L.; Hutter, J. *Phys. Rev. Lett.* **1998**, *80*, 3650.
- (4) Huo, C. F.; Ren, J.; Li, Y. W.; Wang, J. G.; Jiao, H. J. *J. Catal.* **2007**, *249*, 174.
- (5) Andreoni, W.; Varma, C. M. *Phys. Rev. B* **1981**, *23*, 437.
- (6) Xu, Y.; Mavrikakis, M. *J. Phys. Chem. B* **2003**, *107*, 9298.
- (7) Xu, Y.; Ruban, A. V.; Mavrikakis, M. *J. Am. Chem. Soc.* **2004**, *126*, 4717.
- (8) Yim, W.-L.; Klüner, T. *J. Catal.* **2008**, *254*, 349.
- (9) Siaj, M.; Oudghiri-Hassani, H.; Maltais, C.; McBreen, P. H. *J. Phys. Chem. C* **2007**, *111*, 1725.
- (10) Sorescu, D. C.; Rusu, C. N.; Yates, J. T. *J. Phys. Chem. B* **2000**, *104*, 4408.
- (11) Carlisle, C. I.; King, D. A.; Bocquet, M. L.; Cerda, J.; Sautet, P. *Phys. Rev. Lett.* **2000**, *84*, 3899.
- (12) Johnson, K.; Ge, Q.; Titmuss, S.; King, D. A. *J. Chem. Phys.* **2000**, *112*, 10460.
- (13) Fernandez, J. L.; White, J. M.; Sun, Y. M.; Tang, W. J.; Henkelman, G.; Bard, A. J. *Langmuir* **2006**, *22*, 10426.
- (14) Koper, M. T. M.; Shubina, T. E.; van Santen, R. A. *J. Phys. Chem. B* **2002**, *106*, 686.
- (15) Inderwildi, O. R.; Jenkins, S. J.; King, D. A. *J. Phys. Chem. C* **2008**, *112*, 1305.
- (16) Henkelman, G.; Arnaldsson, A.; Jónsson, H. *Comput. Mater. Sci.* **2006**, *36*, 354.
- (17) Yim, W.-L.; Klüner, T. *J. Comput. Chem.* **2008**, *29*, 1306.
- (18) Sanchez-Escribano, V.; Vargas, M. A. L.; Finocchio, E.; Busca, G. *Appl. Catal., A* **2007**, *316*, 68.
- (19) Morgan, G. A.; Kim, Y. K.; Yates, J. T. *Surf. Sci.* **2007**, *601*, 3548.
- (20) Mortensen, J. J.; Hammer, B.; Nørskov, J. K. *Phys. Rev. Lett.* **1998**, *80*, 4333.
- (21) Kim, Y. K.; Morgan, G. A.; Yates, J. T. *Chem. Phys. Lett.* **2006**, *431*, 317.
- (22) Kim, Y. K.; Morgan, G. A.; Yates, J. T. *Chem. Phys. Lett.* **2006**, *422*, 350.



- (23) Pratt, S. J.; King, D. A. *Surf. Sci.* **2003**, *540*, 185.
- (24) Liu, Z. P.; Hu, P. *J. Am. Chem. Soc.* **2001**, *123*, 12596.
- (25) Jenkins, S. J.; King, D. A. *J. Am. Chem. Soc.* **2000**, *122*, 10610.
- (26) Vaari, J.; Lahtinen, J.; Talo, A.; Hautajarvi, P. *Surf. Sci.* **1991**, *251*, 1096.
- (27) Wu, M. C.; Dong, S. Z.; Zhu, A. R. *Surf. Sci.* **1989**, *216*, 420.
- (28) Chen, J. G.; Crowell, J. E.; Ng, L.; Basu, P.; Yates, J. T. *J. Phys. Chem.* **1988**, *92*, 2574.
- (29) Ng, L.; Uram, K. J.; Xu, Z.; Jones, P. L.; Yates, J. T. *J. Chem. Phys.* **1987**, *86*, 6523.
- (30) Paul, J. *Nature* **1986**, *323*, 701.
- (31) Konsolakis, M.; Yentekakis, I. V. *Appl. Catal., B* **2001**, *29*, 103.
- (32) Hammer, B.; Jacobsen, K. W.; Nørskov, J. K. *Surf. Sci.* **1993**, *297*, L68.
- (33) Zhang, J.; Chen, J.; Li, Y.; Sun, Y. *J. Nat. Gas Chem.* **2002**, *11*, 99.
- (34) Nosé, S. *J. Chem. Phys.* **1984**, *81*, 511.
- (35) Kresse, G.; Hafner, J. *Phys. Rev. B* **1993**, *47*, 558.
- (36) Kresse, G.; Hafner, J. *Phys. Rev. B* **1994**, *49*, 14251.
- (37) Kresse, G.; Furthmüller, J. *Phys. Rev. B* **1996**, *54*, 11169.
- (38) Kresse, G.; Furthmüller, J. *Comput. Mater. Sci.* **1996**, *6*, 15.
- (39) Perdew, J. P.; Burke, K.; Ernzerhof, M. *Phys. Rev. Lett.* **1997**, *78*, 1396.
- (40) Kresse, G.; Joubert, D. *Phys. Rev. B* **1999**, *59*, 1758.
- (41) Henkelman, G.; Jónsson, H. *J. Chem. Phys.* **2000**, *113*, 9978.
- (42) Henkelman, G.; Uberuaga, B. P.; Jónsson, H. *J. Chem. Phys.* **2000**, *113*, 9901.
- (43) Reboredo, F. A.; Galli, G. *J. Phys. Chem. B* **2006**, *110*, 7979.
- (44) Ma, Q. M.; Xie, Z.; Wang, J.; Liu, Y.; Li, Y. C. *Phys. Lett. A* **2006**, *358*, 289.
- (45) Lu, X.; Tian, F.; Xu, X.; Wang, N. Q.; Zhang, Q. *J. Am. Chem. Soc.* **2003**, *125*, 10459.
- (46) Xu, L. J.; Henkelman, G.; Campbell, C. T.; Jónsson, H. *Phys. Rev. Lett.* **2005**, *95*, 146103.
- (47) Savin, A.; Jepsen, O.; Flad, J.; ersen, O. K.; Preuss, H.; Vonschnering, H. G. *Angew. Chem., Int. Ed.* **1992**, *31*, 187.
- (48) Bader, R. F. W. *Chem. Rev.* **1991**, *91*, 893.
- (49) Costales, A.; Kandalam, A. K.; Pendas, A. M.; Blanco, M. A.; Recio, J. M.; Pandey, R. *J. Phys. Chem. B* **2000**, *104*, 4368.
- (50) Jensen, F. *Introduction to Computational Chemistry*, 1st ed.; Wiley: West Sussex, 1999.
- (51) Nosé, S. *Mol. Phys.* **1984**, *52*, 255.
- (52) Lu, X.; Zhang, L.; Xu, X.; Wang, N.; Zhang, Q. *J. Phys. Chem. B* **2002**, *106*, 2136.
- (53) Liu, Z.-P.; Hu, P.; Alavi, A. *J. Am. Chem. Soc.* **2002**, *124*, 14770.
- (54) Gong, X. Q.; Raval, R.; Hu, P. *Surf. Sci.* **2004**, *562*, 247.

CT800243Y